

# The Role of Photon Statistics in Fluorescence Anisotropy Imaging

Keith A. Lidke, Bernd Rieger, Diane S. Lidke, and Thomas M. Jovin

**Abstract**—Anisotropy imaging can be used to image resonance energy transfer between pairs of identical fluorophores and, thus, constitutes a powerful tool for monitoring protein homo-association in living single cells. The requirement for only a single fluorophore significantly simplifies biological preparation and interpretation. We use quantitative methods for the acquisition and image processing of anisotropy data that return the expected error of the anisotropy per pixel based on photon statistics. The analysis methods include calibration procedures and allow for a balance in spatial, anisotropy, and temporal resolution. They are featured here with anisotropy images of fluorescent calibration beads and enhanced green fluorescent protein complexes in live cells.

**Index Terms**—Confocal microscopy, energy migration fluorescence resonance energy transfer (emFRET), enhanced green fluorescent protein (eGFP), scale selective filtering.

## I. INTRODUCTION

FLUORESCENCE polarization is extensively used in the study of biochemical and biological molecules in solution. When a fluorescence sample is excited by polarized light, the fluorophores with absorption dipoles parallel to the plane of excitation polarization will be preferentially excited, i.e., in a photoselective manner. The extent of polarization of the emission can be described in terms of the steady-state anisotropy function

$$r = \frac{I_{\parallel} - GI_{\perp}}{I_{\parallel} + 2GI_{\perp}} \quad (1)$$

where  $I_{\parallel}$  and  $I_{\perp}$  are the parallel and perpendicular polarized emission signals, respectively, and  $G$  is a system-dependent factor accounting for the different sensitivities in the detection channels (see Section III-B). Due to the dependence of  $r$  on the rotational correlation time, anisotropy measurements can reveal information about molecular microenvironment (viscosity) and conformational or association state [1]. Another process

Manuscript received December 13, 2004; revised May 18, 2005. This work was supported in part by a TALENT fellowship from the Netherlands Organization for Scientific Research (NWO) and in part by the EU FP5 Project QL2-CT-2001-02278. K. A. Lidke and B. Rieger contributed equally to this publication. The associate editor coordinating the review of this manuscript and approving it for publication was Dr. Robert F. Murphy.

K. A. Lidke, D. S. Lidke, and T. M. Jovin are with the Department of Molecular Biology, Max Planck Institute for Biophysical Chemistry, 37077 Göttingen, Germany (e-mail: k lidke@gwdg.de; d lidke@gwdg.de; t jovin@gwdg.de).

B. Rieger was with the Department of Molecular Biology, Max Planck Institute for Biophysical Chemistry, 37077 Göttingen, Germany. He is now with FEI Electron Optics, 5600 KA Eindhoven, The Netherlands (e-mail: b rieger@nl.feico.com).

Digital Object Identifier 10.1109/TIP.2005.852458

that results in changes in emission polarization is fluorescence resonance energy transfer (FRET) [1], [2]. The measurement of anisotropy in the microscope provides the possibility for studying these phenomena in living cells [1], [3].

FRET results from the dipole–dipole interaction between two fluorophores, the emission spectrum of one (donor, D) overlapping the excitation spectrum of the other (acceptor, A). The strength of this interaction is dependent upon the D–A separation ( $R^{-6}$ ) and is very sensitive in the 2–10 nm range. The ability of FRET to measure such distances has led to widespread use of this technique in the study of molecular interactions and functional states in biological systems. Typically, the FRET D–A pair consists of two spectroscopically distinct species. Recently, there has been renewed interest in using anisotropy in heteroFRET [4]. However, FRET can also occur between identical fluorescent molecules exhibiting a small Stokes' shift, i.e., separation between absorption and emission bands. This energy migration FRET (emFRET) [1], or homoFRET, between like molecules does not alter the ensemble fluorescence intensity, lifetime or spectrum, but results in a depolarization of the population's fluorescence [1], [3], [5], since the orientation of the secondarily excited molecules is uncorrelated with the original orientational distribution established by photoselection. EmFRET has the distinct advantage of requiring only a single fluorophore species. The common use of expression tags, such as enhanced green fluorescent protein (eGFP) [6], renders emFRET an attractive method for studying protein homo-associations in the cell.

Here, we present theoretical and experimental considerations for detecting  $r$  (and emFRET in particular) via measurements of anisotropy in the confocal microscope. Specifically, we describe the fundamental limits of anisotropy resolution based on the total number of detected photons, suggest methods for calibration of an anisotropy imaging system, and describe an imaging procedure for optimizing spatial, temporal, and anisotropy resolution for a given system of interest. We also present a method for automated anisotropy image processing, in which the sensitivities of the two polarization channels are determined automatically from images of the sample so as to generate an optimized anisotropy image. We present results obtained with calibration beads and live cells expressing eGFP.

## II. FUNDAMENTAL UNCERTAINTY OF ANISOTROPY DUE TO PHOTON STATISTICS

In fluorescence, steady-state photon emission and detection obey Poisson statistics, leading to a fundamental uncertainty in

the measured anisotropy (1). Applying standard propagation of error for uncorrelated signals, one obtains the variance in  $r$

$$v(r) = \frac{9G^2 I_{\perp}^2}{(2GI_{\perp} + I_{\parallel})^4} v(I_{\parallel}) + \frac{9G^2 I_{\parallel}^2}{(2GI_{\perp} + I_{\parallel})^4} v(I_{\perp}) + \frac{9I_{\perp}^2 I_{\parallel}^2}{(2GI_{\perp} + I_{\parallel})^4} v(G). \quad (2)$$

Assuming that  $G$  can be determined with arbitrary accuracy, i.e.,  $v(G) = 0$ , and given that for photon statistics, the variance is estimated by the measured value in photon units, e.g.,  $v(I_{\parallel}) = I_{\parallel}$ , and (2) reduces to

$$v(r) = \frac{9G^2 I_{\perp} I_{\parallel} (I_{\perp} + I_{\parallel})}{(2GI_{\perp} + I_{\parallel})^4}. \quad (3)$$

Combining (1) and (3), we arrive at alternative relationships for the variance of  $r$

$$v(r) = \frac{(1-r)^2(1+2r)(1-r+G(1+2r))}{9GI_{\perp}} \quad (4)$$

$$= \frac{(1-r)(1+2r)^2(1-r+G(1+2r))}{9I_{\parallel}} \quad (5)$$

$$= \frac{(1-r)(1+2r)(1-r+G(1+2r))}{3I_{\text{tot}}} \quad (6)$$

where  $I_{\text{tot}} = I_{\parallel} + 2GI_{\perp}$  is the total emission intensity. The standard deviation  $sd(r) = \sqrt{v(r)}$  corresponding to (6) for  $r = 0$  and  $r = 0.4$  (the theoretical maximal anisotropy for an isotropically rotating fluorophore in one-photon excitation [7]) is plotted in Fig. 1. For two-photon excitation, the maximal value for  $r$  is higher (0.57 [8]). The  $sd(r)$  varies inversely with  $\sqrt{I_{\text{tot}}}$  but is only a weak function to  $r$ . The limits are  $0.82/\sqrt{I_{\text{tot}}}$  ( $r = 0$ ) and  $0.93/\sqrt{I_{\text{tot}}}$  ( $r = 0.4$ ) for  $G = 1$ . A typical confocal image corresponds to only tens to hundreds of detected photons per pixel, and the inset of Fig. 1 shows the standard deviation of  $r$  in this range. More photons per pixel can be acquired by averaging a large number of measurements but there is a finite limit imposed by the need to operate within the linear and low (to avoid saturation and photobleaching effects) excitation intensity range and by the time scale of sample dynamics.

### III. SYSTEM SETUP AND CALIBRATION

The system used for these studies was a confocal laser scanning microscope (Zeiss CLSM 310) with 488-nm excitation from an Ar-ion laser, 520–570 nm bandpass emission filter followed by a polarizing beam splitter and two PMTs for the parallel and perpendicular channels. All measurements on the microscope were performed with a  $63 \times 1.2$  NA water objective and were acquired with a back-projected pinhole size of 1 Airy unit.

Anisotropy imaging requires additional calibration beyond the setup and calibration of a typical confocal microscope, as will be discussed in the following sections.

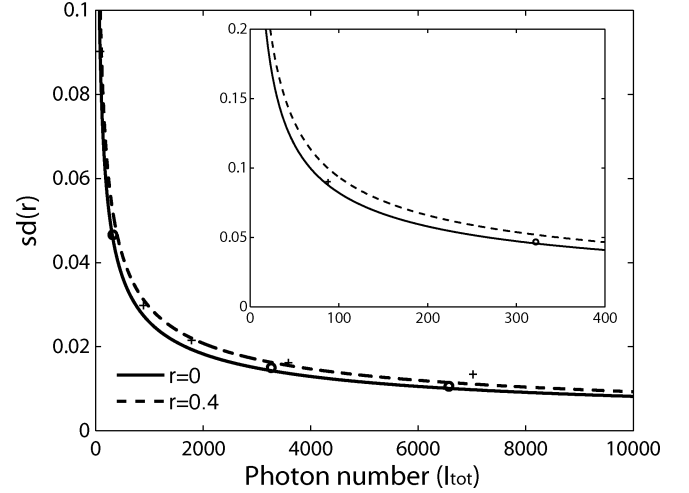


Fig. 1. Dependence of the standard deviation of  $r$  on the total number of detected photons ( $I_{\text{tot}}$ ) for  $G = 1$ . The inset shows the region corresponding to the number of photons in a typical confocal image. Measured standard deviations of fluorescent calibration beads with  $r = 0.04$  ( $\circ$ ) and  $r = 0.14$  ( $+$ ), shown in Figs. 5 and 6. Increasing photon counts were generated by incrementally summing more images in a stack.

#### A. From Signals to Photon Number

All analyses of the expected variance in a measurement due to photon statistics assume that the measured signal intensity is given in collected photon counts. Most instruments do not directly report the actual number of photons collected, but rather a value generated by integrating the analog signals (photocurrents) produced in the photomultiplier tube (PMT). The output signal is given in analog to digital units (ADUs). Therefore, it is necessary to calculate the number of (detected) photons pn from the measured intensity given by the ADUs of the recording device. This conversion is given by the gain factor [9]  $\text{gain} \equiv \text{ADUs}/\text{pn}$  leading to the relations

$$\frac{v(\text{ADUs})}{\text{ADUs}} = \frac{\text{gain}^2 \cdot v(\text{pn})}{\text{gain} \cdot \text{pn}} = \text{gain}. \quad (7)$$

In wide-field imaging, the detector is usually a CCD camera for which statistical evaluations have been extensively developed [9]. In the case of PMTs used for confocal imaging, the gain depends strongly on the operating voltage across the dynode chain, a setting that is often changed to match the brightness of the sample.

A calibration of the detected photon numbers can be made by a procedure based on the equivalence in photon statistics between the noise variance and the mean intensity [9]. A series of images of the same object is recorded, and the resulting intensity variance in each pixel of the series is attributed to the sum of intrinsic fluctuations due to photon statistics and a constant system dependent noise denoted the read noise. For best results, the full dynamic range of the detector up to the point of saturation should be represented in the image. A defocused object is an easy and suitable test image. A background dark level is measured and subtracted from the series. To rule out fluctuations of the light source, one normalizes every image by its integrated intensity. The mean intensity and variance is computed per pixel over the series. A plot of the variance versus intensity yields a line with slope equal to the gain [defined according to (7)], and

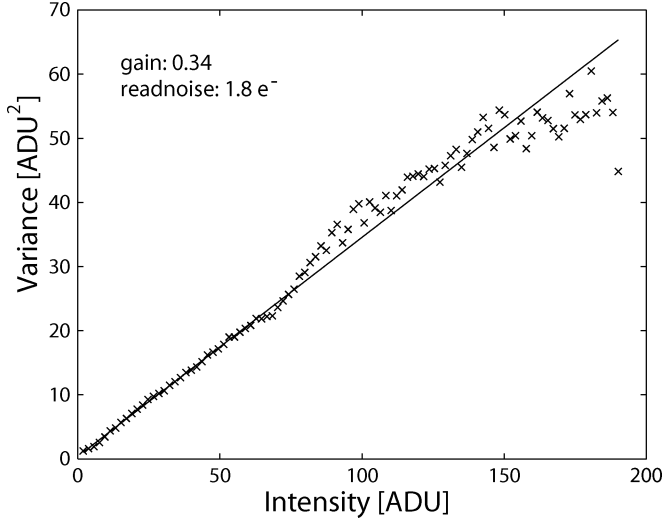


Fig. 2. Calibration of the confocal microscope (Zeiss CLSM 310) for PMT channel  $I_{\parallel}$ .

an intercept from which the read noise of the detector is calculated (typically given in rms  $e^-$ ):  $\text{read noise} = \sqrt{\text{intercept}/\text{gain}}$ .

The number of photons recorded by the detector is not equivalent to the collected photons due to the finite wavelength-dependent quantum efficiency of the detector and multiplicative noise, which also often varies with wavelength [10]. Quantum efficiencies can be estimated by comparison with reference spectra from a spectrofluorometer. Such values are generally supplied by the manufacturer but can vary from device to device and over time [10]. It should be noted that the calibration of the detector gain does not require knowledge of the quantum efficiency, as both the incident and detected photons are Poisson distributed. We used the above technique to calibrate the two PMTs on the confocal microscope. A calibration for the  $I_{\parallel}$  channel at one given voltage is shown in Fig. 2.

### B. $G$ Factor

In general, the detection efficiencies for the different polarization orientations in any system are unequal. To account for this circumstance in the microscope,  $G \equiv I_{\parallel}^0/I_{\perp}^0$  is measured for a sample of known polarization (generally,  $\sim 0$ ). In the spectrofluorometer, with right-angle geometry, the  $G$  factor can be determined from any randomly orientated sample by excitation with polarization parallel to the detection path, as described further in the next subsection. The factor  $G$  derives historically from “grating,” since, in spectrofluorometers, the main polarization dependency stems from the monochromator grating [7]. In a microscope system, the polarization dependency is influenced by the optical path, which may contain many reflective and dielectric surfaces, as well as by the individual detector response.

Ordinarily, the  $G$  factor is calibrated every time a measurement is taken with different PMT voltages. We show below that only one gain-independent  $G$  measurement is required for a particular setup of the microscope and can be used for all PMT settings by first converting ADUs to photon numbers in the acquired images. This procedure only requires knowledge of the PMT gain, which can be measured more easily than the  $G$  factor

(and can be obtained from the image itself without the need for an independent reference sample). Note that the  $G$  factor in the microscope is a mean value over the wavelength range dictated by the emission filter(s), optical transmission factors and detector quantum yield.

### C. Spectrofluorometer Measurements and Objective Depolarization

The anisotropy of a sample in solution is most often measured by a spectrofluorometer, in which the excitation and collection apertures are small, such that the measured values of  $I_{\parallel}$  and  $I_{\perp}$  account accurately for light emitted with polarization direction parallel or perpendicular to the excitation axis, and the denominator of (1) is equivalent to the total emission intensity. Note that for an isotropic sample, there are two perpendicular emission axes that are equal by symmetry but only one is measured, accounting for the factor of 2. However, large optical apertures are characteristic of most microscopes, particularly when using large NA objectives for detection of fluorescence. In such systems, one has to contend with significant depolarization and mixing effects both on excitation and emission [11], [12].

To calibrate our microscope system for these effects, we used a set of fluorescent beads (InSpeck Green, Molecular Probes) designed for intensity calibration in flow cytometry, but that also show a range of concentration-dependent depolarization, presumably due to emFRET. A 10:1 dilution of the beads in water was measured in a spectrofluorometer (Varian Cary Eclipse) equipped with programmable excitation and emission polarizers, using 488-nm,  $\pm 5$  excitation and emission collected from 500–600 nm in 0.5-nm steps with a monochromator slit width of 5 nm. A measurement of unlabeled beads was subtracted from each measurement as a background.

A wavelength-dependent  $G$  factor was calculated for each measurement using a suspension of the brightest beads by excitation with a polarization direction perpendicular to both detection axes. Due to symmetry, the sample should emit equal intensities in the two detection channels, allowing the determination of  $G$ . Equation (1) takes on the form

$$r = \frac{I_{VV} - \frac{I_{HV}}{I_{HH}} I_{VH}}{I_{VV} + 2 \frac{I_{HV}}{I_{HH}} I_{VH}} \quad (8)$$

where  $V$  and  $H$  correspond to polarization directions vertical and horizontal with respect to the instrumental frame, respectively, and in  $I_{XY}$ ,  $X$  and  $Y$  denote excitation and emission, respectively [13].

For each PMT setting used in the spectrofluorometer, the ADU-to-photon conversion was performed using the method described in Section III-A, and the anisotropy ( $r_i$ ) and its variance ( $v_i$ ) was calculated for every wavelength ( $\lambda_i$ ), according to (9), shown at the bottom of the next page, in which all the signals were wavelength dependent. A mean value of  $r$ ,  $\langle r \rangle$ , was calculated over the wavelength range  $\lambda_i$  ( $\lambda_i = 520$  nm,  $\lambda_n = 570$  nm, corresponding to the band pass filter used in the microscope)

$$\langle r \rangle = \frac{\sum_{i=1}^n r_i}{\sum_{i=1}^n \frac{1}{v_i}} \quad (10)$$

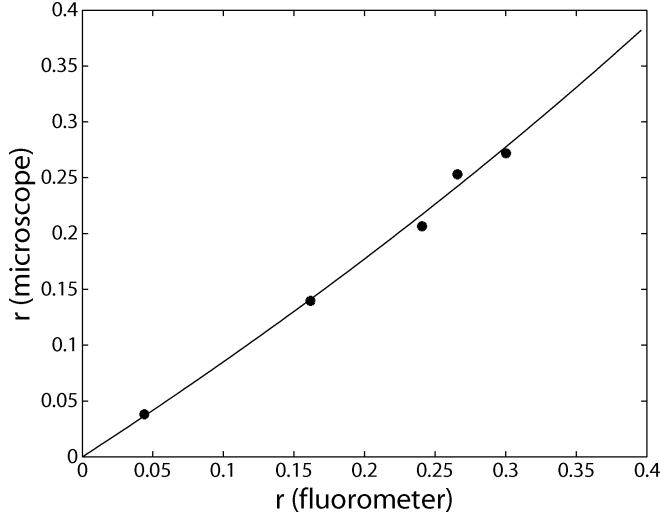


Fig. 3. **Anisotropy measurement of five sets of InSpeck Green calibration beads in the spectrofluorometer and CLSM.** The microscope values show a depolarization due to the finite aperture of excitation and collection. The standard deviations in both the microscope and fluorometer measurements were smaller than the displayed point size. Beads are labeled by the manufacturer with respect to the brightest beads. The respective anisotropy values for 100%, 30%, 10%, 3%, 1% InSpeck beads (Lot #63B1-4) are  $0.0440 \pm 0.0012$ ,  $0.1616 \pm 0.0013$ ,  $0.2407 \pm 0.0015$ ,  $0.2658 \pm 0.0028$ ,  $0.3002 \pm 0.0036$  measured in the spectrofluorometer, and  $0.0381 \pm 0.00003$ ,  $0.1397 \pm 0.00008$ ,  $0.2065 \pm 0.0001$ ,  $0.2530 \pm 0.00007$ ,  $0.2718 \pm 0.0001$  measured in the microscope. The fit line was derived as explained in the text.

where the corresponding variance of  $\langle r \rangle$  is

$$v(\langle r \rangle) = \frac{1}{\sum_{i=1}^n \frac{1}{v_i}}. \quad (11)$$

In general, the  $G$  spectrum can be fit to a smooth function characterizing the system in order to reduce the  $G$  factor contribution to the variance of  $\langle r \rangle$ . We did not apply this procedure. The same beads were prepared for measurement in the microscope by drying  $10 \mu\text{l}$  of undiluted sample onto a coverslip. The dried coverslip was mounted on a slide with a drop of water and sealed with nail polish. A series of images was taken of each bead type to check for photobleaching. Signals from all beads and all images were combined to yield a total photon count for the parallel and perpendicular channels.

The anisotropy value was calculated from the total signal, and the standard deviation using (3). The anisotropy measured in the microscope is plotted versus the anisotropy measured in the spectrofluorometer in Fig. 3. In principle, the anisotropy values measured in the microscope can be corrected for the depolarization effects of the objective. Aperture correction parameters were calculated according to [6], fitting the data to  $r(\text{microscope}) = (-r - 2br)/(-3a + 2r - 2br)$ , where  $r$  is  $r(\text{fluorometer})$ . A fit to the data in Fig. 3 yields the values  $a = 0.83$  and  $b = 0.51$ . In this study, we present the uncorrected microscope anisotropy values.

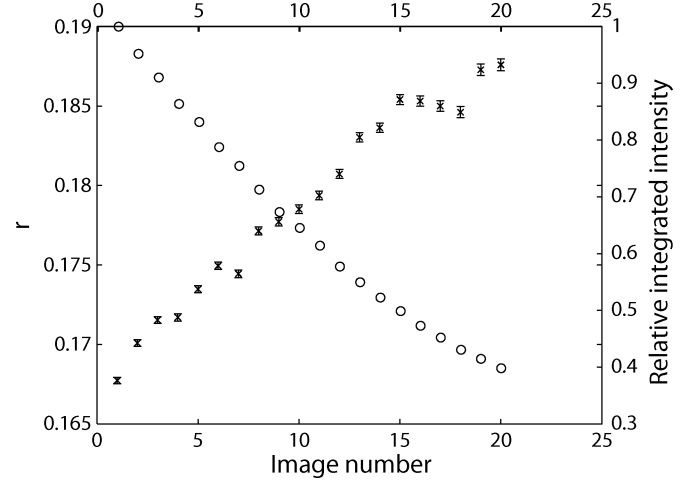


Fig. 4. **Mean anisotropy of a HeLa cell expressing a cytoplasmic dimeric eGFP construct.** The value increases as photobleaching effectively converts dimeric tandem complexes to monomers. After each imaging scan, a scan with the full laser intensity was performed corresponding to an illumination equivalent to five imaging scans. Circles (o) indicate the total intensity of the cell normalized to the initial intensity. Crosses (x) indicate the mean anisotropy and are given with error bars denoting the standard deviation  $sd(r) = \sqrt{v(r)}$  where  $v(r)$  is found using (6).

#### D. Avoidance of Saturation

The analysis of anisotropy is based on the assumption that the probability of excitation of all fluorophores in the system is proportional to the square of the dot product between the excitation polarization vector and the fluorophore excitation dipole vector ( $\cos^2\theta$  relationship [7]). However, due to the finite lifetime of fluorophores, this assumption is not fulfilled when  $1/(\sigma\tau)$  approaches  $\Psi$ , where  $\Psi$  is the photon flux,  $\sigma$  is the absorption cross-section, and  $\tau$  is the fluorophore lifetime. Fluorescence saturation manifests itself as a nonlinear response of the fluorophore to excitation intensity, leading to an apparent decrease in measured anisotropy. This condition may easily be reached in a confocal microscope. Thus, before experiments are performed, the response of the system to excitation intensity should be measured over 1–2 orders of magnitude and an intensity selected for the anisotropy experiments that is well within the linear regime. We have performed this measurement on both the calibration beads and live HeLa cells expressing eGFP used in this study, and found a linear response up to the maximum excitation irradiance of our microscope. This result is expected in view of  $\sigma$  for eGFP ( $9 \times 10^{-17} \text{ cm}^{-2}$  [14]),  $\tau = 3 \text{ ns}$ , and the estimated maximum  $\Psi$  at the sample of  $\Psi = 2 \cdot 10^{23} \text{ photons/cm}^2/\text{s}$  compared to  $1/(\sigma\tau) = 4 \cdot 10^{24} \text{ photons/cm}^2/\text{s}$ .

#### E. Minimizing the Effect of Photobleaching

If the application of anisotropy imaging is to spatially resolve molecular monomers from dimers or multimers, it is important to determine the photobleaching rate and its effect on

$$v_i(r) = \frac{9I_{HH}I_{HV}I_{VH}I_{VV}(I_{HH}I_{HV}I_{VH} + I_{HV}I_{VH}I_{VV} + I_{HH}I_{VV}(I_{HV} + I_{VH}))}{(2I_{HV}I_{VH} + I_{HH}I_{VV})^4} \quad (9)$$

the sample under study. A greater number of fluorophores in a multimer exhibiting homoFRET generally results in a lower anisotropy due to the increased probability of transfer [15]. Photobleaching reduces the number of fluorophores within the multimer, thus increasing the anisotropy [15], [16]. Fig. 4 shows the mean anisotropy in a time series of a HeLa cell containing cytoplasmic eGFP tandem constructs [3]). After each image in the time series, the cell was intentionally photobleached with an illumination dose corresponding to five imaging scans. As the cell progressively photobleached, the anisotropy tended toward the measured monomer value of  $r = 0.23$  (see Section V). Based on this information, the total excitation dose of the sample was reduced to the point where the change in anisotropy due to photobleaching was small compared to the desired resolution in anisotropy. This procedure should be observed when acquiring a single image or when following dynamic behavior over a time series.

#### IV. PROCEDURE FOR IMAGE ACQUISITION AND PROCESSING

After system calibration, the anisotropy per pixel is computed in accordance with (1); the variance is given by (6). However, anisotropy images acquired in a confocal microscope will generally exhibit a large standard deviation, and it may be difficult to discern regions with distinct anisotropy values.

Here, we will describe how to achieve a balance between spatial, anisotropic, and temporal (if applicable) resolution based on filtering the  $I_{\parallel}$  and  $I_{\perp}$  images before computation of the anisotropy  $r$ . The acquired channels must be first smoothed and subsequently divided, and not first divided and then smoothed, as for two variables  $x, y$  the ratio  $\langle x \rangle / \langle y \rangle$  is an unbiased estimation in the asymptotic limit, whereas  $\langle x/y \rangle$  is not [17].

As is evident from Fig. 1, the standard deviation diminished rapidly with an increasing number of detected photons. Thus, by averaging pixels and increasing  $I_{\text{tot}}$ , the  $r$  image becomes less noisy, albeit with some loss in spatial resolution, if neighborhood filters are employed. The expectation is that the gain in  $r$  resolution will outweigh the loss in spatial resolution, particularly in the highly nonlinear region of (2) (Fig. 1). Thus, even with a linear filter, one can reap the benefits of nonlinear selectivity.

As a first test, we imaged a mixture of two different calibration beads ( $r = 0.04$  and  $r = 0.14$ , Figs. 5 and 6), acquiring a time series of 80 images. The beads also differed in intensities. The anisotropy and the variance of the anisotropy from the effective number of photons were computed over 1, 10, and 80 exposures. The gain was computed from the images directly for conversion of the ADUs to photons. The gain estimation was in good agreement (less than 5% error) with a calibration image. Depending on the images, the calculated gain may have too high an error to be used as the only estimate of the  $G$  factor acquired. In this case, a separate calibration series should be taken, or a direct measurement of the  $G$  factor. As shown in Fig. 5, using only one time frame results in an anisotropy image with an extremely high variance. By averaging increasing numbers of time frames, the variance decreases and the anisotropy difference between the two species becomes evident. However, this effect yields diminishing returns as a

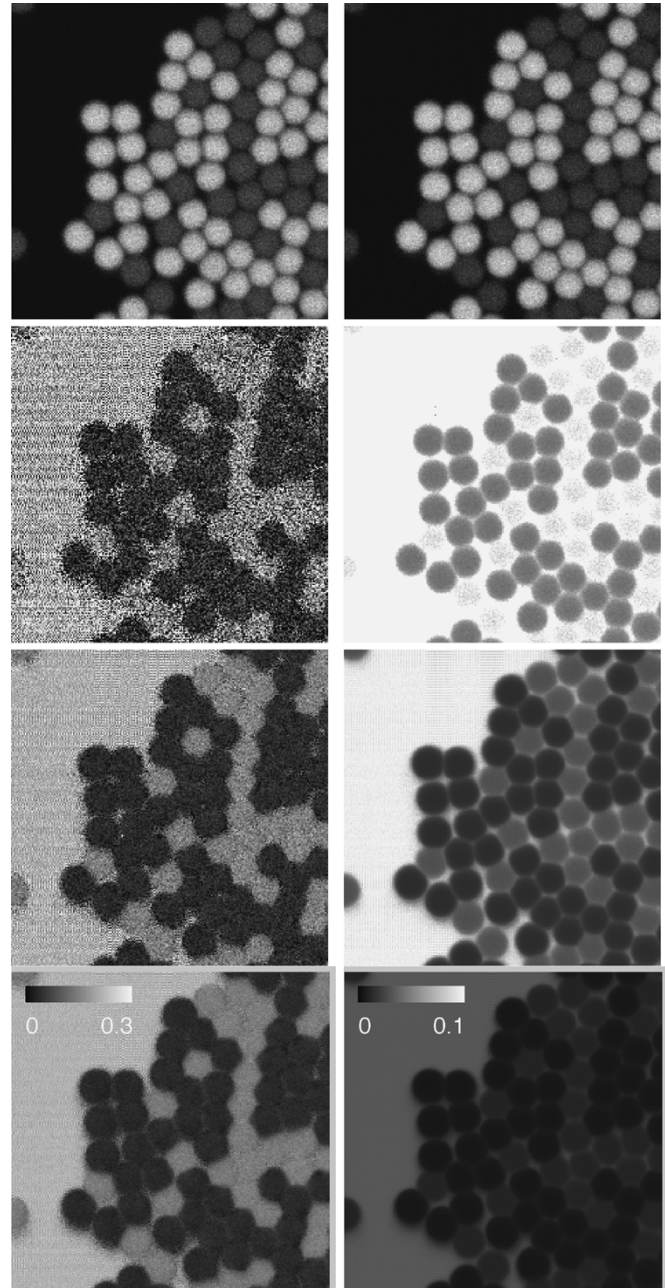


Fig. 5. **Effect of increasing the effective number of photons on the anisotropy image and standard deviation.** Top row: The acquired images. Left:  $I_{\parallel}$ . Right:  $I_{\perp}$ . Below (left column) anisotropy images  $r$  (display range [0, 0.3]) and (right column) expected standard deviation due to photon statistics as (2) (display range [0,0.1]). A pixel uncertainty above 0.1 is considered unusable for all applications. Top to bottom: Averages over 1, 10, and 80 exposures. The effective photon numbers per pixel are for the brighter, darker beads  $\sim 350$  and 80, respectively, for one time frame and multiples thereof with the number of time frames. The beads have a diameter of  $2.5 \mu\text{m}$  and the darker ones have a higher anisotropy. The “ripples” in the noise are due to aligning of the time series with sub-pixel precision shift in the Fourier domain.

function of the number of included images, as can be seen from the nonlinear dependency of (2).

Spatial resolution can also be exchanged for anisotropy resolution. We investigated the effect of isotropic Gaussian filtering of the images  $I_{\parallel}$  and  $I_{\perp}$  before evaluation of (1). In Fig. 6, we show the effect of spatial filtering on the same series of bead images for a Gaussian width  $\sigma = 1, 2$ , and 4. Fig. 7 shows the ex-

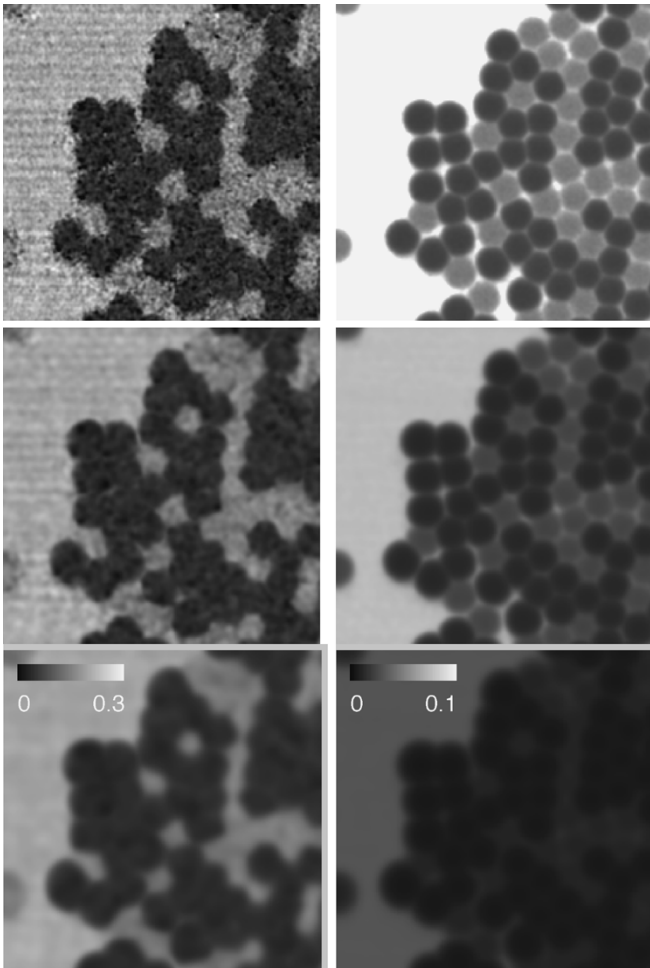


Fig. 6. **Effect of spatial filtering on anisotropy image and standard deviation.** Left column: Anisotropy images  $r$  (display range [0, 0.3]). Right column: Expected standard deviation due to photon statistics as (2) (display range [0,0.1]). A pixel uncertainty above 0.1 is considered inadequate for all applications. From top to bottom: Gaussian width  $\sigma = 1, 2, 4$ . The effective photon numbers for the {brighter, darker} beads are {1400;350}, {5500;1500},  $\{2 \cdot 10^4; 5000\}$ , whereas for the unfiltered image the numbers are {350;80}. The beads had a diameter of  $2.5 \mu\text{m}$ .

pected improvement on the uncertainty of the anisotropy based on an average of 50, 100, 200, and 500 photons per pixel in the footprint of the filter against the size of the Gaussian width  $\sigma$  for two-dimensional (2-D) filtering. For clarity, we only show curves for  $r = 0.4$  and  $G = 1$ . The effective number of pixels averaged by a Gaussian filter  $1/(2\pi\sigma^2)^{n/2} \int dx^n e^{-x^2/2\sigma^2}$  of scale  $\sigma$  is  $(2\pi\sigma^2)^{n/2}$ , where  $n$  is the dimensionality. The size of the footprint of a Gaussian is infinite and only truncated (here at  $3\sigma$ ) for the implementation, but the effective number is given by the normalization of the Gaussian as the pixel values in the footprint are weighted. For example, a uniform filter in 2-D of size  $3 \times 3$  corresponds to nine pixels, and a Gaussian with scale  $\sigma = 1$  to about six pixels. In any case, Gaussian filters [18], [19] are to be preferred over the (still commonly used) uniform filter as the Gaussian is isotropic and optimizes the tradeoff between spatial and frequency domain localization [20]. For low photon numbers, the benefits of spatial averaging can be significant. In Figs. 7 (2-D filtering) and 8 [three-dimensional (3-D) filtering], we only plot values of  $\sigma \geq 0.9$  as for lower  $\sigma$  the appropriate sampling condition for band-limitation of a Gaussian

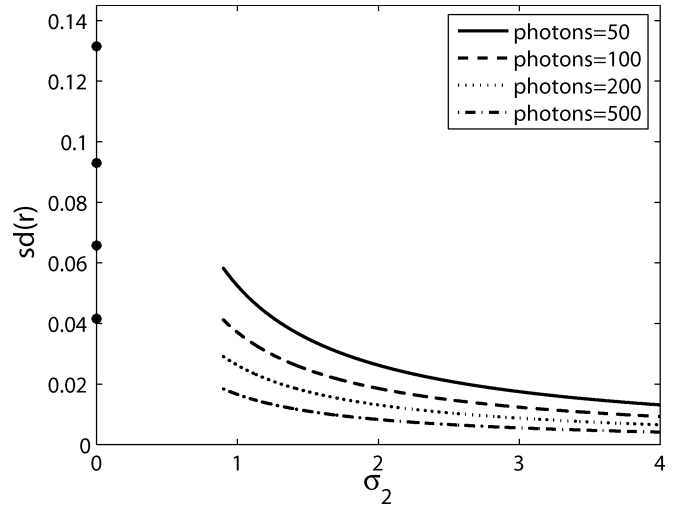


Fig. 7. **Uncertainty  $sd(r)$  of the anisotropy based on 50, 100, 200, and 500 effective photons per pixel in the footprint of the filter against the size of the Gaussian width  $\sigma_2$  for 2-D ( $r = 0.4$  and  $G = 1$ ).** The unfiltered value of  $sd(r)$  is given on the ordinate axis.

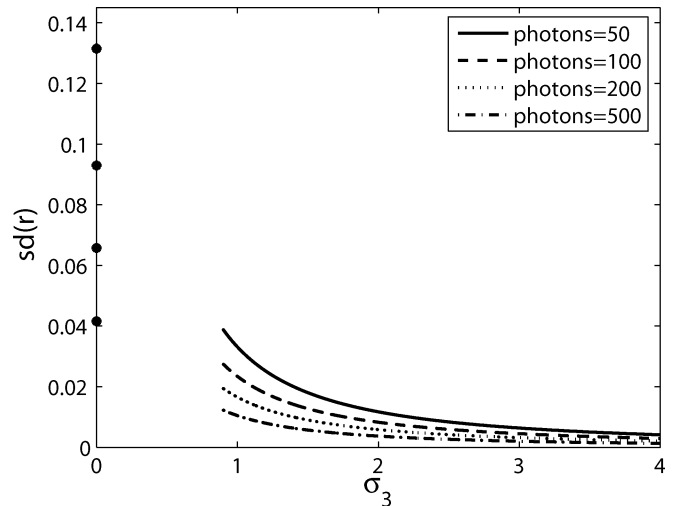


Fig. 8. **Uncertainty  $sd(r)$  of the anisotropy based on 50, 100, 200, and 500 effective photons per pixel in the footprint of the filter against the size of the Gaussian width  $\sigma_3$  for 3-D ( $r = 0.4$  and  $G = 1$ ).** The unfiltered value of  $sd(r)$  is given on the ordinate axis.

is not fulfilled [21]. Smaller  $\sigma$  can be achieved via convolution in the Fourier domain if necessary [20].

If a time series can be acquired, the temporal resolution can be exchanged for spatial resolution or simply for  $r$  resolution by taking the mean along the time axis. The images must be first aligned to correct for lateral drift in the microscope. Temporal averaging is to be preferred over spatial filtering if the scene is static to prevent blurring in the spatial dimension while increasing anisotropy resolution. If the object of interest is dynamic and images can be acquired at a higher rate than the (biological) process, spatiotemporal filtering of the 3-D- $(x, y, t)$  image can provide significant benefits, as can be seen in Fig. 8, which shows the expected uncertainty of the anisotropy based on an average of 50, 100, 200, and 500 photons per pixel in the footprint of the 3-D filter against the Gaussian width  $\sigma$ .

### A. Filtering for Constant Anisotropy Resolution

We can assign an uncertainty value to every pixel in the anisotropy image. However, to detect small spatial or temporal changes in  $r$ , it is sometimes desirable to compute an image with constant uncertainty, i.e., a constant  $sd(r)$ , or alternatively a constant coefficient of variation (CV, standard deviation divided by the mean). This can be achieved by building a Gaussian scale space with its strong causality constraint [19], [22] from the two input images  $I_{\parallel}$  and  $I_{\perp}$ . The target standard deviation or CV can be compared to the computed one at a certain scale and for the pixels that match the criterion the anisotropy value is stored along with the respective scale. The scale selection can be performed with some prior knowledge. A rough estimate of the Gaussian smoothing required to achieve the target criterion can be calculated based on the needed number of effective photons (Figs. 7 and 8 for 2-D and 3-D filtering, respectively). For greater smoothing, we use a fast recursive implementation of the Gaussian filter [23].

One might wish to use an adaptive filter instead of an isotropic Gaussian to average only pixels with similar anisotropies. Unfortunately, one cannot apply a (generalized) Kuwahara filter [24], which is otherwise possible in cases where the feature for steering the filter can be generally computed, as, e.g., for orientation [25]. In the case of anisotropy, steering cannot be based on the intensities of  $I_{\parallel}$ ,  $I_{\perp}$ , or  $I_{\text{tot}}$  because, in most cases, the anisotropy supplies contrast that is simply not evident in the intensity images alone.

### B. Automated Procedure

We assume that the  $G$  factor and the gain are measured under the instrumental conditions of the measurement, that is, there is a single  $G$  factor that characterizing the system. A protocol for automated anisotropy imaging is the following.

- 1) Acquire a stack of  $I_{\parallel}$  and  $I_{\perp}$  images.
- 2) Acquire a background image using current PMT settings.
- 3) Compute the gain from the images, thus converting ADUs to effective photon numbers and allowing the PMT voltage independent  $G$  factor to be used.
- 4) Choose a target anisotropy uncertainty or target CV.
- 5) Choose between 2-D and 3-D filtering.
- 6) Choose constant spatial/temporal or constant anisotropic resolution.
- 7) Apply automated selection of the corresponding filter kernel size per pixel (for constant  $r$  uncertainty or CV) or based on a fixed kernel average photon number (for constant spatial resolution).
- 8) Generate images showing the anisotropy and the variance or scale space.

In rare cases, the gain estimation from the image may fail if only a small range of gray values is represented in the image, in which case a calibration image must be acquired as described above. This approach is still advantageous compared to a measurement of the  $G$  factor, which requires a separate unpolarized sample. For the gain estimation, any stack of images with a gradient will suffice.

## V. ANISOTROPY IMAGING IN LIVING CELLS

To demonstrate anisotropy imaging on a biological sample, we imaged HeLa cells expressing either monomeric, dimeric, or trimeric eGFP complexes. The anisotropy decreased from monomer ( $r = 0.22$ ) to dimer ( $r = 0.19$ ) to trimer ( $r = 0.16$ ), indicative of increasing degrees of emFRET as the number of eGFPs in a complex increased. Recovery of anisotropy to the monomer values was observed upon photobleaching the dimer and trimer complexes (as seen for the dimer in Fig. 4).

To demonstrate the ability to discern anisotropy differences in a living sample, we imaged A431 cells expressing the eGFP dimer complex in the presence of epidermal growth factor (EGF) coupled to 525-nm emitting Quantum Dots (EGF-QD525s) [26] (Fig. 9). EGF-QD525s bind to the endogenous membrane receptor erbB1 (the classical EGF Receptor, EGFR) on A431 cells, activate the receptor, and induce its internalization [26]. QD525s have an emission spectrum that greatly overlaps the emission of eGFP, making spectral discrimination difficult. However, good contrast between these signals can be achieved in two ways. The first is by exploiting the large lifetime differences between QD525s and eGFP [27]. The second approach is based on the near-zero anisotropy of QD525s emission compared to the significant anisotropy of eGFP, as demonstrated below.

We incubated A431 cells expressing the eGFP dimer complex ( $r = 0.19$ ) with EGF-QD525s and imaged the anisotropy over time. The locations of the quantum dots (QDs) were easily discerned from the eGFP background using image processing based on the differences in anisotropy. After 15 min of incubation at room temperature, corresponding to the initial phases of binding and internalization, the EGF-QD525 covers the cell (observed as a lower anisotropy, i.e., a darker rim, at the cell periphery in the anisotropy image). Regions of accumulation in cytoplasmic endosomes were easily distinguished by the near zero anisotropy [Fig. 9(c), left panel]. The effective photon number per pixel was so low for one confocal time slice (less than 15 photons) that no useful information could be obtained directly from the raw data due to this uncertainty dictated by the photon statistics.

A comparison of different image processing methods is shown in Fig. 9(b), filtering for constant anisotropy resolution for  $sd(r) = 0.02$  in 2-D, and in Fig. 9(c), for  $sd(r) = 0.01$  in 3-D. Note the larger scales needed for 2-D filtering to achieve an even lower standard deviation of 0.02 than for 3-D filtering of 0.01. Larger scales in turn imply lower resolution [compare the two left images of Fig. 9(b) and (c)]. For the 3-D filtering, separated clusters of QDs are observed. In panels Fig. 9(d) and (e), the filtering procedures for constant  $CV(r) = 0.25$  in 2-D and 3-D, respectively, were applied. An interesting point is the occurrence of larger scales at the location of the QDs as opposed to the smaller scales for the constant  $sd(r)$  filtering. The cause was the very low (near-zero) anisotropy at these loci, such that only a very low standard deviation yielded the target CV ( $sd/\text{mean}$ ). The value of the anisotropy in panel d is greater than in the other anisotropy images, as many neighboring pixels' values with high anisotropy were averaged in order to achieve the high number of effective photons required by the

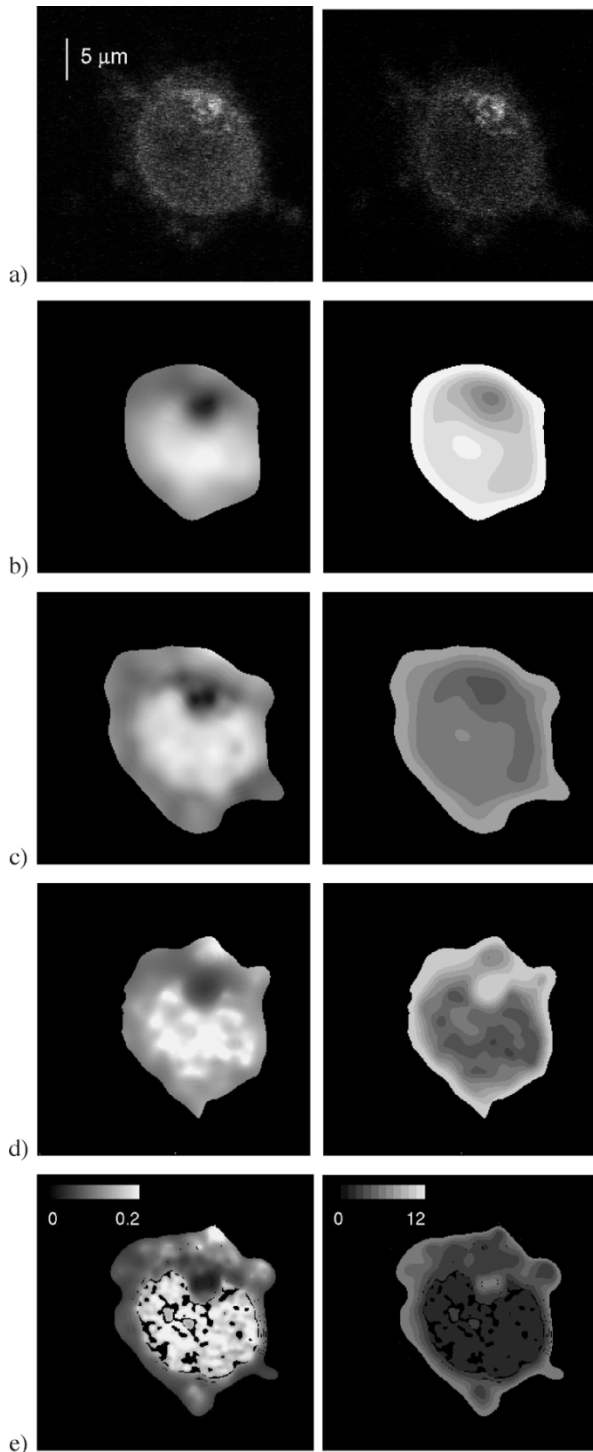


Fig. 9. Images from a single confocal section through the center of the cell. (a) Intensity images. Left:  $I_{\parallel}$ . Right:  $I_{\perp}$ . For panels (b)–(e), the left column shows anisotropy images (display range [0, 0.2]) and the right column is the scale image, width  $\sigma$  of the Gaussian per pixel (display range [0, 12]). (b) Constant anisotropy uncertainty filtering in 2-D for  $sd(r) = 0.02$ . (c) Constant anisotropy uncertainty filtering in 3-D for  $sd(r) = 0.01$ . (d) Constant anisotropy CV filtering in 2-D for  $CV(r) = 0.25$ . (e) Constant anisotropy CV filtering in 3-D for  $CV(r) = 0.25$ . For an explanation of the differences of (b)–(e), see text. The “black holes” in (e) are due to overly coarse scale space sampling. The scale to meet the target criterion with a certain tolerance is skipped and, therefore, no value is assigned. To remove the “holes,” a finer scale sampling or a larger tolerance can be used.

target CV. For 3-D filtering, this requirement is less severe as the scale can be smaller.

## VI. CONCLUSION

Contrast in a fluorescence intensity image, which is sufficient for many explorations in the microscope, does not guarantee an adequate resolution in an anisotropy image. To quantitate this effect, we have derived relationships for the minimum uncertainty in an anisotropy measurement based on the number of total collected photons, and applying filtering with a 2-D or 3-D Gaussian kernel. These results have been employed in combination with system calibration to generate an automated image processing routine that returns an anisotropy image calculated with a constant  $\sigma$ , constant anisotropy standard deviation, or constant coefficient of variation. Also generated are images of the estimate of standard deviation in the case of constant  $\sigma$  filtering, or a  $\sigma$  scale map in the case of constant  $sd(r)$  and constant  $CV(r)$  filtering. These image processing routines have been demonstrated both with calibration beads and live cells demonstrating ligand binding and receptor internalization. Our approach for estimating expected errors per pixel can and should be applied to any imaging suffering from low photon numbers that returns results only after applying mathematical operations on the raw data, such as the calculation of FRET efficiency or anisotropy. The propagation of error will be different for each case and may lead to different trends as seen in Figs. 1, 7, and 8. However, this approach gives rise to a valid quantitative interpretation of the obtained values.

## ACKNOWLEDGMENT

The authors would like to thank R. Heintzmann for helpful discussions and for reading the manuscript. The eGFP tandem constructs were the kind gift of P. I. H. Bastiaens and the calculations were performed with the MATLAB toolbox DIPImage [28].

## REFERENCES

- [1] A. H. A. Clayton, Q. S. Hanley, D. J. Arndt-Jovin, V. Subramaniam, and T. M. Jovin, “Dynamic fluorescence anisotropy imaging microscopy in the frequency domain (rFLIM),” *Biophys. J.*, vol. 83, no. 3, pp. 1631–1649, 2002.
- [2] E. A. Jares-Erijman and T. M. Jovin, “FRET imaging,” *Nature Biotechnol.*, vol. 21, no. 7, pp. 1138–1395, 2003.
- [3] A. Squire, P. J. Verwee, O. Rocks, and P. I. H. Bastiaens, “Red-edge anisotropy microscopy enables dynamic imaging of homo-FRET between fluorescent proteins in cells,” *J. Struct. Biol.*, vol. 147, no. 1, pp. 62–69, 2004.
- [4] A. L. Mattheyses, A. D. Hoppe, and D. Axelrod, “Polarized fluorescence resonance energy transfer microscopy,” *Biophys. J.*, vol. 87, no. 4, pp. 2787–2797, 2004.
- [5] I. Gautier, C. Tramier, J. Coppey, R. B. Pansu, J.-C. Nicolas, K. Kemnitz, and M. Coppey-Moisan, “Homo-FRET microscopy in living cells to measure monomer-dimer transition of GFP-tagged proteins,” *Biophys. J.*, vol. 80, no. 6, pp. 3000–3008, 2001.
- [6] V. Subramaniam, Q. S. Hanley, A. H. A. Clayton, and T. M. Jovin, “Photophysics of green and red fluorescent proteins: some implications for quantitative microscopy,” *Meth. Enzymol.*, vol. 360, pp. 178–201, 2003.
- [7] B. Valeur, *Molecular Fluorescence*. Weinheim, Germany: Wiley-VCH, 2002.
- [8] I. Gryczynski, H. Malak, and J. R. Lakowicz, “Three-photon induced fluorescence of 2,5-diphenyloxazole with a femtosecond Ti:sapphire laser,” *Chem. Phys. Lett.*, vol. 245, no. 1, pp. 30–35, 1995.
- [9] L. J. van Vliet, D. Sudar, and I. T. Young, *Cell Biology*, 2nd ed. New York: Academic, 1998, vol. III, pp. 109–120.

- [10] H. Illers, E. Buhr, D. Bergmann, and C. Hoeschen, "Measurement of the detective quantum efficiency (dqe) of digital x-ray imaging devices according to the standard iec 62 220-1," *Proc. SPIE*, vol. 5368, pp. 177–187, 2004.
- [11] D. Axelrod, "Fluorescence polarization microscopy," *Meth. Cell Biol.*, vol. 30, pp. 333–352, 1989.
- [12] K. Bahlmann and S. W. Hell, "Depolarization by high aperture focusing," *Appl. Phys. Lett.*, vol. 77, no. 5, pp. 612–614, 2000.
- [13] J. R. Lakowicz, *Principles of Fluorescence Spectroscopy*, 2nd ed. New York: Kluwer, 1999.
- [14] G. H. Patterson, S. M. Knobel, W. D. Sharif, S. R. Kain, and D. W. Piston, "Use of green fluorescent protein and its mutants in quantitative fluorescence microscopy," *Biophys. J.*, vol. 73, no. 5, pp. 2782–2790, 1997.
- [15] L. W. Runnels and S. F. Scarlata, "Theory and application of fluorescence homotransfer to melittin oligomerization," *Biophys. J.*, vol. 69, no. 4, pp. 1569–1583, 1995.
- [16] D. S. Lidke, P. Nagy, B. G. Barisas, R. Heintzmann, J. N. Post, K. A. Lidke, A. H. A. Clayton, D. J. Arndt-Jovin, and T. M. Jovin, "Imaging molecular interactions in cells by dynamic and static fluorescence anisotropy (rFLIM and emFRET)," *Biochem. Soc. Trans.*, vol. 31, no. 5, pp. 1020–1027, 2003.
- [17] G. M. P. van Kempen and L. J. van Vliet, "Mean and variance of ratio estimators used in fluorescence ratio imaging," *Cytometry*, vol. 39, no. 4, pp. 300–305, 2000.
- [18] D. Marr and E. Hildreth, "Theory of edge detection," in *Proc. Roy. Soc. Lond. B*, vol. 207, 1980, pp. 187–217.
- [19] J. J. Koenderink, "The structure of images," *Biol. Cybern.*, vol. 50, pp. 363–370, 1984.
- [20] A. Papoulis, *Signal Analysis*. New York: McGraw-Hill, 1977.
- [21] P. W. Verbeek and L. J. van Vliet, "On the location error of curved edges in low-pass filtered 2-D and 3-D images," *IEEE Trans. Pattern Anal. Mach. Intell.*, vol. 16, no. 7, pp. 726–733, Jul. 1994.
- [22] T. Lindeberg, "Scale-space for discrete signals," *IEEE Trans. Pattern Anal. Mach. Intell.*, vol. 12, no. 3, pp. 234–254, Mar. 1990.
- [23] I. T. Young and L. J. van Vliet, "Recursive implementation of the Gaussian filter," *Signal Process.*, vol. 44, no. 2, pp. 139–151, 1995.
- [24] M. Kuwahara, K. Hachimura, S. Eiho, and M. Kinoshita, "Processing of ri-angiocardigraphic images," *Digital Process. Process. Biomed. Images*, pp. 187–203, 1976.
- [25] P. Bakker, L. J. van Vliet, and P. W. Verbeek, "Edge preserving orientation adaptive filtering," in *Proc. Conf. Computer Vision and Pattern Recognition*, vol. 2, Los Alamitos, CA, 1999, pp. 535–540.
- [26] D. S. Lidke, P. Nagy, R. Heintzmann, D. J. Arndt-Jovin, J. N. Post, H. Grecco, E. A. Jares-Erijman, and T. M. Jovin, "Quantum dot ligands provide new insights into erbB/HER receptor-mediated signal transduction," *Nature Biotechnol.*, vol. 22, no. 2, pp. 198–203, 2004.
- [27] H. Grecco, K. A. Lidke, R. Heintzmann, D. S. Lidke, C. Spagnuolo, O. E. Martinez, E. A. Jares-Erijman, and T. M. Jovin, "Ensemble and single particle photophysical properties (two-photon excitation, anisotropy, FRET, lifetime, spectral conversion) of commercial quantum dots in solution and in live cells," *Microsc. Res. Tech.*, vol. 65, no. 3, pp. 169–179, 2004.
- [28] C. L. Luengo Hendriks, B. Rieger, M. van Ginkel, G. M. P. van Kempen, and L. J. van Vliet, "DIPimage: A scientific image processing toolbox for MATLAB," Delft Univ. Technol., Delft, The Netherlands. [Online] Available: <http://www.qi.tnw.tudelft.nl/DIPlib>, 1999.



**Keith A. Lidke** received the Ph.D. degree in physics from the University of Minnesota, Minneapolis, in 2002.

He is currently a postdoctoral researcher at the Max Planck Institute for Biophysical Chemistry, Göttingen, Germany. His research interests include the development and application of quantitative fluorescence microscopy.



**Bernd Rieger** received the M.Sc. degree in physics from the Munich University of Technology, Munich, Germany, in 1999, and the Ph.D. degree in image processing and analysis from the Delft University of Technology, Delft, The Netherlands, in 2004.

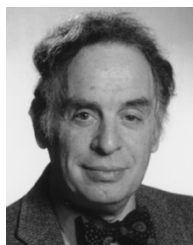
He spent one-and-a-half years as a postdoctoral researcher at the Max Planck Institute for Biophysical Chemistry, Göttingen, Germany. Currently he is with FEI Electron Optics, Eindhoven, The Netherlands. His research interests include the development of greyvalue-based estimators for the analysis of

structure in images.



**Diane S. Lidke** received the Ph.D. degree in biophysical sciences and medical physics from the University of Minnesota, Minneapolis, in 2002.

Currently, she is a postdoctoral researcher at the Max Planck Institute for Biophysical Chemistry, Göttingen, Germany. Her research interests include the application of fluorescence spectroscopy and microscopy techniques to the study of protein dynamics/interactions during signal transduction.



**Thomas M. Jovin** received the M.D. degree from the Johns Hopkins University, Baltimore, MD, in 1964.

A scientific member of the Max Planck Society since 1969, he has served as director of the Department of Molecular Biology at the Max Planck Institute for Biophysical Chemistry, Göttingen, Germany, since the Institute's inception in 1971.